Guided Plasma Jets Directed Onto Wet Surfaces: Angular Dependence and Control

Guy Parsey[1,3], Amanda M. Lietz[2] and Mark J. Kushner[1,4]

[1] Department of Electrical Engineering and Computer Science, University of Michigan, 1301 Beal Avenue, Ann Arbor, MI 48109-2122, USA

[2] Sandia National Laboratories, Applied Optical and Plasma Sciences Department, 1515 Eubank Blvd. SE, Albuquerque, NM 87185, USA

[3] Present Address: KLA Corp., 2350 Green Rd #100, Ann Arbor, MI 48105, USA

[4] Author to whom correspondence should be addressed

E-mail: guy.parsey@kla.com, amlietz@sandia.gov, mjkush@umich.edu

Abstract

The optimal use of atmospheric pressure plasmas jets (APPJs) for treatment of surfaces – inorganic, organic and liquid – depends on being able to control the flow of plasma-generated reactive species onto the surface. The typical APPJ is a rare gas mixture (RGM) flowed through a tube to which voltage is applied, producing a RGM plasma plume that extends into the ambient air. The RGM plasma plume is guided by a surrounding shroud of air due to the higher electric field required for an ionization wave (IW) to propagate into the air. The mixing of the ambient air with the RGM plasma plume then determines the production of reactive oxygen and nitrogen species (RONS). The APPJ is usually oriented perpendicular to the surface being treated. However, the angle of the APPJ with respect to the surface may be a method to control the production of reactive species to the surface due to the change in APPJ propagation properties and the resulting gas dynamics. In this paper, we discuss results from computational and experimental investigations addressing two points – propagation of IWs in APPJs with and without a guiding gas shroud as a function of angle of the APPJ with respect to the surface; and the use of this angle to control plasma activation of thin water layers. We found that APPJs propagating out of the plasma tube into a same-gas environment lack any of the directional properties of shroud-guided jets, and largely follow electric field lines as the angle of the plasma tube is changed. Guided APPJs propagate coaxially with the tube as the angle is changed, and turn perpendicularly towards the surface only a few mm above the surface. The angle of the APPJ produces different gas dynamic distributions, which enable some degree of control over the content of RONS transferred to thin water layers.

I. Introduction

Atmospheric pressure plasma jets (APPJs) as used for materials processing or biotechnology applications are often operated in rare gases (or rare gases with small percentages of a molecular gas) flowing into ambient air [1,2]. A typical configuration is a dielectric tube with internal or external electrodes (or a combination of the two) through which the rare gas mixture (RGM) is flowed. Voltage pulses are applied at a few to tens of kHz. With internal diameters of a few mm and flow rates of a few slm, the flow speed of the RGM exiting the tube is up to a few thousand cm/s. When flowing into the ambient air, a plume of the RGM is formed surrounded by a shroud of air. With application of the voltage pulse, an ionization wave (IW) is produced in the tube, which then propagates through the plume of RGM extending into the ambient. Since the E/N (electric field/gas number density) required to sustain the IW in the RGM is lower than that of the surrounding air, the IW is usually confined to the RGM. As ambient air diffuses into the RGM plume, the E/N required to sustain the ionization wave increases, until the IW can no longer propagate. The confinement of the ionization wave to the RGM plume has motivated describing these plasma jets as *guided streamers* or *guided ionization waves* [3]. This description acknowledges that the propagation of the IW is shaped or guided to remain in the RGM plume due to the lower E/N required for propagation in the plume compared to the surrounding air.

The mechanism producing *guided ionization waves* is well illustrated by the optical imaging of emission from OH in turbulent APPJs. Iseni et al. [4] imaged APPJs sustained in argon propagating into ambient air. OH emission was produced by the IW interacting with water impurities in the RGM and with water vapor from the humidity of the air. As the RGM plume transitioned from laminar to turbulent, the OH emission was observed in the rare gas dominated portions of the turbulent plume. Xian et al. showed that the confinement of the plasma depends on the composition of the surrounding gas, with molecular gases providing more confinement because of electron energy losses to vibrational and rotational excitation [5]. Lietz et al. [6] used computer simulations to investigate a He APPJ propagating into air where the RGM plume developed large scale vortices that produce regions dominated by rare gas and dominated by air. The propagating IW was largely confined to the rare gas dominated portions of the turbulent plume.

The majority of the experimental and computational investigations of APPJs interacting with surfaces have the plasma jet oriented perpendicular to the surface. In this configuration, the RGM plume produces a stagnation point directly under the jet which directs the flow of the RGM radially outwards in a rare gas dominated boundary layer above the surface. Depending on the flow speed, Reynolds number and flow of the ambient air, a sheer layer is created between the RGM plume and the ambient which may produce vortices. The dynamics of the vortices are important in mixing the ambient air with the RGM dominated plume and with the boundary layer through which the IW wave propagates. The mixing of air into the RGM plume and into the path of the IW is important to the production of reactive oxygen and nitrogen species (RONS) which is often the desired product of the APPJ. The flow dynamics are not independent of the discharge. Experimental observations have shown that depending on operating conditions (e.g.,

flow rate and voltage polarity), a laminar flow without a discharge can be tripped into turbulent flow when the discharge operates. The opposite trend has also been observed [7,8,9]. The dependence of flow on discharge properties extend to the type of surface being treated – metal, dielectric or liquid [10].

When an APPJ is incident at normal incidence onto a dielectric or low conductivity surface, the surface is charged by the IW. The charging of the surface produces horizontal components of the electric field, which then aids in the propagation of the ionization wave along the surface in the RGM dominated boundary layer [11,12,13]. Due to the electric enhancement that occurs at the dielectric interface of the material, this surface ionization wave (SIW) can be more intense than the original IW that propagates through the RGM plume [14]. The SIW can be responsible for the production of the majority of RONS. This is particularly the case for APPJs incident onto wet surfaces or water solutions. In these cases, the SIW propagates through high humidity in the boundary layer, generating ROS (reactive oxygen species) due to electron impact dissociation of the water vapor in the boundary layer. There can be significant differences in the reactive fluxes to the surface depending on whether the active plasma plume touches or does not touch the surface [15].

If the APPJ is directed onto the surface at a non-normal angle, several systematic trends occur. First, the dynamics of the RGM plume after striking the surface will be a function of the angle of incidence of the jet. As the angle deviates from the normal, the stagnation point becomes weaker and flow along the surface follows more from the advective flow of the plume and less from pressure gradients produced by the stagnation point. Stronger shear forces may be produced, generating larger vortices that mix the ambient air with the RGM plume. The RGM preferentially flows along the surface in the direction of the angled jet. The guided streamer will then preferentially propagate through those parts of the plume, boundary layer and vortices that are dominated by the RGM. The end result is that the guided streamer preferentially propagates in the direction of RGM flow, asymmetrically along the surface.

There have been few systematic studies of the consequences of APPJs striking surfaces at non-normal incidence. Damany et al. [16] investigated an argon APPJ propagating into air and onto a glass plate with the plasma tube oriented at 0°, 45° and 65° from the vertical. At an angle of 65°, increasing the gas flow extended the position at which the IW intersected with the plate. The resulting SIW extended further downstream (in the direction of gas flow) at higher flow rates. At an angle of 45°, time-resolved ICCD imaging showed that the IW and plasma plume remained coaxial with the plasma tube. When approaching within 1-2 mm of the surface, the IW and plasma plume turned to being nearly normal to the surface. The resulting SIW propagated dominantly in the direction of gas flow.

Nishime, et al. [17] investigated He APPJ treatment of polyethylene terephthalate (PET) polymer as a function of angle of incidence, from normal to grazing. They found that the area of the PET with a reduced water-contact-angle, usually attributed to oxygen-containing functional groups on the surface produced by the plasma jet, was a sensitive function of the angle of the jet. This treated area was maximum at an APPJ angle of 45°. When treating a starch-iodine-agar plate as a technique to detect ROS, the treated area elongated by a factor of 2.5-3 as the APPJ

transitioned from normal to nearly grazing angle. The low activation at normal incidence was attributed to the stagnation flow blocking oxygen species from the ambient from mixing with the plasma, whereas grazing angles enabled more mixing of the ambient gas with the plasma plume. Other studies of the angle of the APPJ include an argon jet treating silver films to affect grain size by Hosseinpour et al. [18]. They found that the grain size and surface roughness could be tuned by treating sequentially with the APPJ oriented at different angles.

Another important consequence of APPJs striking a dielectric surface at non-normal incidence is in the charging of the surface. Slikboer et al. [19] investigated charging of a dielectric surface by a He APPJ at normal and 45° incidence, showing significant downstream charging in the direction of flow.

Nearly all manner of interaction of APPJs with surfaces (charging, flow field, mixing with ambient) are functions of the angle of incidence of the jet. This dependence suggests that the angle of the APPJ with respect to the surface could be used as a control mechanism to, for example, treat a surface or activate a liquid.

In this paper, we discuss results from a computational investigation of a He APPJ propagating into ambient air, directed onto dielectric surfaces having a thin water layer, as a function of angle of the APPJ with respect to the surface. The intent of this investigation is to quantify consequences of the angle of the APPJ on the guiding nature of the IW by the ambient air shroud, RONS production and activation of the water layer. We found that a slanted He APPJ in the absence of an ambient gas shroud will largely follow the direction of the vacuum electric fields when leaving the plasma tube, although the IW and the plasma column it produces deforms those electric fields. Ultimately the IW is directed perpendicularly to the surface. When operating as a guided streamer (He APPJ flowing into ambient air), the IW propagates within the shrouded RGM plume, along the extended axis of the tube. The IW is not uniformly distributed in the plume and is shifted towards the ground side of the shroud. Upon approaching within a few mm of the surface, the IW turns towards the vertical. The IW behavior is in agreement with experimental measurements of optical emission. The gas dynamics resulting from the angle of the APPJ affect generation of ROS and RNS differently due to the ROS being dominantly primary reactive species and RNS being secondary reactive species. This difference in dependences on angle then provides some ability to control the ratio of RNS to ROS transferred to the water layer using angle of the APPJ as a control actuator.

Brief descriptions of the model and experiment are in Section II. A discussion of the propagation of non-guided IWs produced by a He APPJ flowing into a He ambient as a function of the angle of the APPJ is in Section III. The propagation of a He APPJ into ambient air onto a thin water layer as a function of angle of incidence is discussed in Section IV. The use of angle as a control mechanism for activating water layers is discussed in Section V. Our concluding remarks are in Section VI.

II. Description of the Model and Geometry, and Experiment

The model used in this investigation, *nonPDPSIM*, and its algorithms for plasma-liquid interactions, have been previously discussed in detail in Refs. [20,21,22]; and so only a brief

description will be given here. *nonPDPSIM* is a 2-dimensional plasma hydrodynamics model executed on an unstructured mesh. Continuity equations for charged particles are formulated using Sharfetter-Gummel fluxes and source functions addressing heavy particle and electron impact processes. The charged particle continuity equations and Poisson's equation for the electric potential are simultaneously integrated using an implicit algorithm. Electron temperature is obtained from a conservation equation for electron energy density. Electron impact rate coefficients and transport coefficients are obtained from solutions of a 2-term spherical harmonic expansion of Boltzmann's equation for the electron energy distribution. Solutions of Boltzmann's equation are produced over a range E/N (electric field/gas number density) which produces a table of rate coefficients as a function of electron temperature, T_e. This table is then interpolated during execution of the code, and updated as conditions change. Photoionization of gas phase and liquid species is also included. All transport equations are solved both in the gas phase and in the liquid, albeit with a different reaction mechanism and transport coefficients.

The gas flow field is produced by solution of a compressible form of the Navier-Stokes equations which has been reformulated to be functions of number density as opposed to mass density. Neutral and charged species then diffuse within this advective flow field. Within the thin water layer addressed here, transport is only by drift-diffusion in the electric field produced by solution of Poisson's equation. Evaporation of the water into the gas phase is accomplished by holding the gas phase density of H_2O at the surface of the liquid equal to that of the saturated vapor pressure. Diffusion of H_2O into the flow field then naturally occurs.

As described in Refs. [21,23], transport of neutral species into (or out of) the water is limited by Henry's law equilibrium at the surface. If the density of the liquid phase species at the surface of the liquid is less than saturated with respect to the gas phase density (that is, the density is lower than the Henry's law equilibrium value), transport from the gas to the liquid for that species is allowed. If the density of the liquid species at the surface of the liquid is super-saturated with respect to the gas phase species (that is, the density is higher than the Henry's law equilibrium value), then transport of that species is allowed from the liquid into the gas. The reaction mechanism used in this investigation for He plasma jets into humid air interacting with water is essentially the same as described in Ref. [24].

The model is 2-dimensional in Cartesian coordinates. Therefore the APPJ is best described as a slot jet. The slot-flow has important differences from the 3-dimensional flow fields that result from an angled cylindrical jet onto a surface. With a 2D slot, the flows on either side of jet are physically isolated by the jet tube itself, whereas in 3D, the gas could flow around the plasma tube. When the flow exits the tube, this isolation of flow on either side of the plume persists. The plumes resulting from 2D slot flow are typically less stable than their 3D cylindrical analogues due to the greater emphasis on shear forces. So in assessing the results of this study, the reader should consider the outcomes as best-case (or worst-case) scenario. We expect that otherwise identical studies in 3D would produce similar trends but would quantitatively be different.

The geometry used in this investigation is shown in Fig. 1. The computational domain is 2.8 cm wide and 1.5 cm tall. The depth of the domain is 1.3 mm, however this depth has no

consequence on the calculation other than to calculate flow speeds based on specified flow rates. The tube of the jet extends into the domain from the top surface at an angle θ_J with respect to the normal. ($\theta_J = 0$ corresponds to a jet directed normal to the surface.) The internal width of the quartz tube is 1.6 mm and the width of the tube walls is 0.5 mm. At normal incidence, the end of the tube is 0.75 cm above the bottom surface. As the angle of the jet is increased, the end of the tube remains at essentially the same location, which then moves the top of the tube to the left in the schematic. The unstructured meshes had a refinement of 40-50 μm in the regions where the plasma was expected to propagate (in the path of the RGM plume and in the boundary layer) and contain cells as large as 500 μm in the surrounding gas flow.

For investigations of unguided streamers, the entire computational domain consists of a He/O_2 mixture of = 99.8/0.2 at 1 atm. There is no injection or pumping of gas. For investigations of guided streamers, a He/O_2 = 99.8/0.2 mixture flows through the tube at 3.2 slm, which produces an average flow speed inside the tube of 2,960 cm/s. Gas outlets are on either side of the computational domain and extend 1 cm above the surface. The boundary condition on the surface of the outlets is a constant pressure at 1 atm. Humid air ($N_2/O_2/H_2O$=79.5/20/0.5) flows through the top surface at rates that depend on the angle of the jet to produce a downward vertical flow speed at the top surface of 35 cm/s.

The applied voltage consists of a –15 kV pulse with 100 ns duration, having a 5 ns rise time and 20 ns fall time. The voltage is applied to an internal electrode centered on the axis of the tube which is 0.5 mm wide and 2 mm long with a rounded end, and aligned parallel to the tube at all angles. The bottom surface of the domain is grounded. For studies of unguided APPJs, the ground plane is covered by a 200 μm dielectric having a relative permittivity of $\varepsilon/\varepsilon_0 = 80$. For studies of guided APPJs, the ground plane is covered by a 200 μm water layer containing 8 ppm dissolved O_2 which evaporates into the ambient. The method of simulating multiple pulses is the same as described in Refs. [20,21].

The experimental setup [25] differs from the model in several ways, but still demonstrates the effect of angle of incidence on the plasma jet. The APPJ was made of two coaxial quartz tubes. He flows through the central tube at 1000 sccm, where the plasma propagates, and 500 sccm of N_2 flows through the outer tube to form a gas shroud. The inner tube has an inner diameter of 2 mm and an outer diameter of 4 mm. The shroud tube has an inner diameter of 10.5 mm and an outer diameter of 12.7 mm. An annular spacer made of poly ether ketone (PEEK) with 8 holes, each 1 mm in diameter, was used to distribute the N_2 flow and keep the two tubes coaxial. The annular powered electrode is inside the central tube and the ground electrode is Cu tape wrapped around the outside of the central tube. The design of the plasma jet is discussed in detail in Ref. [25].

The plasma jet flows into a vacuum chamber, so the gas flow is isolated from any air currents in the laboratory, and the pressure and composition of the surrounding gas can be controlled. The chamber pressure was 600 Torr, and the gas is pumped through a cylindrically symmetric pumping manifold. The plasma jet was directed at an alumina disc 650 μm thick and 2.54 cm in diameter. The jet was produced by a Spellman SL600 power supply and a Directed Energy Inc. DEI PVX-4110 pulse generator with a +7.5 kV pulse having a 100 ns rise time, a

140 ns fall and 395 ns total duration. The jet was pulsed at 1 kHz. The light emitted from the plasma as the IW propagated was observed using an Andor iStar ICCD camera with a 5 ns gate. The alumina target was placed normal to the jet, and at angles of approximately 22° and 45° compared to the axis of the plasma jet. The alumina target was backed with a conductive film, which was grounded.

III. Propagation of Unguided Streamers as a Function of Angle

Unguided streamers were computationally investigated as a function of angle of the plasma tube (θ_J = 0° to 51°). For these cases, the entire computational domain is filled with the He/O_2=99.8/0.2 gas mixture. The electron densities for jets oriented at θ_J = 6°, 28°, 40° and 51° are shown in Fig. 2 for the time at which the IW strikes and charges the dielectric surface. Maximum electron densities that occur in the tube and at the intersection of the IW with the surface are 3-4 × 10^{12} cm^{-3}. The electron impact ionization source S_e and electric potential contours for different times during propagation of the IW are shown in Fig. 3 for θ_J = 6° and 51°.

To a large degree, the guiding of IWs is determined by the local value of E/N required to sustain propagation of the ionization wave. If the surrounding gas of a RGM plume requires a larger E/N to sustain the ionization wave, the wave will not enter the surrounding gas regardless of the direction of the electric field. In the absence of the shrouding gas (that is, in a uniform gas volume), the direction of the IW is in large part determined by the direction of the applied electric field. (Here we are limiting the discussion to conditions in which branching of ionization waves will not occur.) These are the trends displayed by the simulations of unguided APPJs propagating into the He/O_2 ambient. For near-normal incidence, the IW inside the tube propagates nearly symmetrically along the axis of the tube. With the IW charging the inside surface of the tube and with electric field enhancement at the dielectric interface, SIWs also develop along the inside surfaces of the tube. For moderate angle (θ_J < 15-20°), the charging of the tube is sufficient to reorient the local electric fields to remain parallel to the tube and the IW wave propagates symmetrically.

As the IW emerges into the ambient beyond the confinement of the tube, the IW expands laterally and reorients its direction to be aligned with the local electric field, propagating perpendicularly to the potential contours. The conductive plasma column produced by the IW lowers the electric field within the column, producing curvature in the applied potential contours which produces electric field enhancement at the head of the IW. This increasing electric field accelerates the IW as it approaches the surface. The IW strikes the surface at essentially normal incidence to align with the electric field vectors that are initially largely perpendicular to the dielectric surface.

As θ_J increases and the plasma tube is oriented further from the vertical, the IW wave within the tube no longer propagates symmetrically. With this being a negative discharge, the IW propagates towards and along the lower (left) surface of the tube opposite the direction of the applied electric field. With sufficient angle of the tube, the charging of the inside surface of the tube is unable to shield out the direction of the applied electric field and the electric field inside the tube is not parallel to the inside surface of the tube. The plasma inside the tube then

propagates largely as a SIW hugging the lower, left side. In approaching the end of the tube, there is additional electric field enhancement at the rounded edge of the tube that produces a local increase in ionization rates. This electric field enhancement results from the polarization of a round dielectric in an axial electric field. Upon exiting the tube, the IW is quickly reoriented to propagate perpendicularly to the electric potential contours and towards the vertical. The shorting of the electric potential by the conductive plasma column tends to make the electric potential contours flatter and electric field direction more vertical as the IW propagates towards the surface. Even for the most angled jet, θ_J =51°, the IW propagates nearly vertically within 3-4 mm of the end of the tube.

A measure of the guiding (or lack of guiding) of the IW is the displacement of the IW when striking the surface. The displacement is the difference in position from the location at which the IW wave strikes the surface, and the projection of the axis of the plasma tube. This projection is a line on the axis of the tube extended to the surface. An IW wave that propagates in the direction of the axis of the tube all the way to the surface would have a displacement of 0 mm. The displacements of unguided IWs are shown in Fig. 4 as a function of angle of the tube. In the absence of guiding, the IW strikes the surface within a few mm of the lateral location of the end of the tube. So the displacement is nearly the same as the distance to the projection.

IV. Propagation of Guided Streamers as a Function of Angle

Guided streamers or IW were simulated by having the He/O_2 = 99.8/0.2 rare gas mixture propagate into the humid air ambient while varying the angle of the plasma tube, θ_J. In these parameterizations, the grounded lower surface was covered by a 200 μm thick water layer that evaporates into the ambient.

The procedure for these cases is to start with stagnant humid air outside the tube and the RGM flowing through the tube. Flow of the RGM was initialized with the analytic solution of a plane impinging jet followed by a shear transform with an off-axis center flow line [26,27]. While this configuration is not the final state of the flow field, its use in initializing the flow significantly reduced the required runtime to obtain the fully-developed flow field. Without the voltage being applied or seed electrons, the flow of RGM through the tube and humid air from the top plane were turned on, and the fluid equations were integrated until the flow fully developed. After the flow developed, the seed electrons were inserted and voltage was applied to start the IW. Having said that, there is no guarantee that the 2D slot-flow will achieve a true steady state as the flow is intrinsically unstable. That is, the flow will continually shed vortices and create new vortices. So some judgement was required as to when the flow was stable enough to launch the IW. The fluid flow field was computed for 24 ms prior to launching the IW. This resulted in some scatter in the data (see below) because at that instant, the vortex shedding and growth for different jet angles happened to be at different stages. In this study, simulations were not performed over long enough periods of time to average the vortex production and shedding to reduce the scatter.

Even in 3D, this same production and shedding of vortices occurs and leads to pulse-to-pulse variation in plasma properties. The plasma properties appear far more uniform when averaged

over many pulses. These trends are made clear by the imaging of Iseni et al. [4]. When captured by short-gate ICCD imaging, the optical emission from an Ar APPJ shows pulse-to-pulse variations that coincide with the IW propagating through large scale turbulence and vortices. When averaged over many pulses, the optical emission appears to be nearly symmetric and aligned with the axis.

The gas flow fields at the time of applying the voltage pulse for θ_J = 6°, 28° and 40° are shown in Fig. 5. The images are for the densities of He (with flow streamlines superimposed), O_2, and water vapor. For the near normal incidence, θ_J = 6°, the near vertical flow from the tube produced a stagnation point at the water surface under the tube, which directs flow fairly uniformly in both lateral directions. A helium dominated boundary layer is created along the water surface. Ambient O_2 diffuses into the boundary layer, producing a partial pressure of 12 Torr of O_2 at the surface of the water under the jet. The boundary conditions left-and-right for the flow are the same (1 cm high pump port) however the distance to the pump ports are different left-and-right. With the 1 atm enforced boundary condition closer on the left side, a vortex close to the RGM plume is formed. With the 1 atm boundary condition further from the RGM plume on the right side, a severe vortex forms further from the plume.

The boundary condition for evaporating water from the surface is to hold the water density constant at the surface of the water at value corresponding to the vapor pressure. At 300 K, the water vapor pressure is 27 Torr or a density of 8.6×10^{17} cm^{-3}. This source of water vapor diffuses into the boundary layer. The layer of water vapor is *compressed* by the incident jet at the stagnation point, and extends further into the boundary layer as the flow proceeds away from the stagnation point.

As θ_J increases and the jet deviates from the normal, the stagnation point weakens. The flow streamlines emerging from the jet (which in large part track where the He is going) have a smoother transition to flow parallel to the surface on the right side of the tube while creating tighter vortices on the left side. With θ_J increasing, the length of the RGM plume prior to reaching the surface also increases, which provide a longer time for the shear forces between the plume and ambient to pump energy into vortices. This slows the lateral speed of the flow, enabling more O_2 to reach the water and more water vapor to mix with the vortex on the left side. On the right side, the flow streamlines become more parallel to the surface, reducing residence time and reducing mixing with the ambient.

The electron density for the RGM flowing into ambient for jet angles of θ_J = 6°, 22°, 28°, 34°, 40° and 45° are shown in Fig. 6 at the time that the IW strikes and begins to charge the water surface. The superimposed single black contour line is where the He density is 90% of the total – or the molecular gas density is 10% of the total. The electron impact ionization source, S_e, representing the IW, is shown for different times in Fig. 7 for θ_J = 6° and 45°. The figures also have voltage contours as black lines and dotted-dashed line where the molecular gas density is 10% of the total. The maximum electron densities are 3-8 $\times 10^{12}$ cm^{-3}, and occur either at the electrode or upon intersection of the IW with the water layer. For small and moderate values of θ_J (< 20-25°), the IW is strictly contained within the RGM plume. The IW and the plasma column it creates follow the projection of the axis of the tube, as does the RGM plume. The IW

largely propagates in the center of the plume. It is only within a few mm of the surface that the IW is directed vertically by the local electric field. In the absence of charging produced by the plasma, the potential contours are essentially parallel to the water surface. Due to the spreading of the RGM plume along the boundary layer on the surface, there is a larger volume that is dominated by the RGM. The IW is then able to reorient itself toward the vertical while propagating within an RGM dominated gas.

The propagation of the IW inside the tube is nearly the same as for the unguided IWs. The amount of back diffusion of ambient gases into the tube is negligible. As with the unguided IW, as θ_J increases, the IW and plasma begin to hug the left side of the tube in response to the average direction of the applied electric field. Unlike the unguided waves, upon exiting the tube the plasma column and IW continue nearly parallel to the axis of the tube, confined to that part of the flow that has a He fraction greater than 90% (molecular gas fraction less than 10%). As θ_J increases, the IW and plasma column hug the left boundary of the RGM plume near the molecular gas 10% contour. With increasing θ_J, the ambient electric field increasingly accelerates the ionization wave more perpendicular to the plume. However, the electric field is not large enough to enable the IW wave to penetrate into the ambient beyond the molecular gas 10% contour where a larger E/N is required to propagate.

As θ_J increases beyond 35-40°, the IW and plasma plume cross over the molecular gas 10% contour as the surface is approached. That is, the IW propagates, at least partly, into the ambient gas. At these large angles, E/N > 90 Td above the surface of the water, which is sufficient for the IW wave to propagate through the He diluted air.

With these being negative IWs, surfaces in contact with the plasma charge negatively, and negative charge surrounds the plasma column in the ambient. The negative charge surrounding the plasma column is in large part in the form negative ions since electrons rapidly attach to O_2 and dissociatively attach to H_2O in the moderate E/N at the edges of the plume, particularly after the IW has passed. The charge dynamics of the propagation of the guided IW with $\theta_J = 45°$ are demonstrated by the electric field vectors shown in Fig. 8. In these images, the color contours represent the electron density at 10, 20, 30 and 40 ns. The red line is the 10% contour of molecular gases. The vectors represent the direction and magnitude of the electric field. At 10 ns, the IW has yet to exit the tube and has a maximum electron density of 3.2×10^{11} cm^{-3}, slanted towards the left side of the tube. The electric field vectors are in large part oriented with their vacuum configuration as there has been little charging of the surface of the tube and the IW has yet to fully develop. The E/N at the exit of the tube is 45 Td with the vector electric field directed towards the negatively biased electrode. At 20 ns, the IW has developed as a wall hugging surface wave. The lower surface of the tube has charged negatively, producing a positive space charge sheath at its surface, indicated by the electric field vectors pointing into the wall of the tube. With the formation of the conductive plasma column, the electric field vectors inside the tube are directed parallel to the walls with E/N ≈ 15 Td. The IW is sustained by a charge density at the leading edge producing E/N ≈ 75 Td, sufficient to avalanche the RGM. Ahead of the IW, the electric field vectors are largely unchanged from their vacuum values.

At 30 ns, the plasma column has extended 2 mm beyond the end of the tube, confined by the

molecular gas 10% contour. The sheath on the inside surface of the tube (outwardly directed electric field vectors) extends to the end of the tube. Electric field vectors within the plasma column are parallel to the direction of propagation of the IW, aligned with the axis of the tube, with E/N of 10-20 Td. The E/N at the leading edge of the IW is 65-70 Td. As the plasma column propagates, it appears to be a conductive volume that extends the cathode potential into the ambient. Electric field vectors naturally orient themselves to be perpendicular to the surfaces of conductors, and this response occurs here. The electric field vectors outside the plasma column are reoriented towards being normal to the conductive plasma column. The E/N beyond the 10% molecular gas contour does not 80 exceed Td, which is well below the E/N required to avalanche humid air (120-130 Td) and so the IW is prevented from propagating into the ambient.

At 40 ns, the IW has reached within 1 mm of the surface and is beginning to turn towards the vertical. The electric field vectors inside the plasma column continue to be aligned with the direction of the IW with values of 15-25 Td. With the compression of the applied potential in front the conductive plasma column, the E/N outside the molecular gas 10% contour increases to as high as 90-100 Td, thereby enabling the IW to penetrate more deeply into the helium diluted molecular gas. Electric field vectors in the ambient are oriented nearly perpendicularly to the plasma column on the left (lower) side where the plasma density exceeds 10^{12} cm^{-3}. On the right (upper) surface, the plasma density is a few 10^{11} cm^{-3} and the plasma column is proportionally less conductive. As a result, the ambient electric field vectors intersect the column at less normal angles.

The displacement of the guided IW wave is shown in Fig. 4. Two values of displacement are shown – when the ionization wave strikes the water surface and 2.5 mm above the surface. The displacement of the guided wave when striking the surface is about half that of the unguided wave. This small displacement demonstrates the confining effects of the humid-air shroud around the RGM plume. However, the majority of this displacement occurs in the last 2.5 mm of propagation when the stagnation flow produces a large volume of RGM dominated gas, and the electric field intensifies as the plasma column approaches the ground plane. The displacements of the guided jets 2.5 mm above the surface are small, indicated strong confinement by the humid air shroud.

The predicted trends for guided IWs striking surfaces at angles agree well with experimental observations. For example, Damany et al. [16] investigated APPJs sustained in argon flowing into ambient air at 20 kHz incident onto dielectric surfaces at varying angles. They found that for $\theta_J = 45°$ with the opening of the tube 5.5 mm above the surface, the air shroud of the RGM plasma plume guided the IW coaxially with the tube until about 1.5 mm above the surface. At this height, the IW turned to strike the surface at a near normal incidence. (See Fig. 6 of Ref. [16].)

ICCD imaging, shown in Fig. 9, was performed of a He APPJ striking a 650 μm thick alumina ($\varepsilon_r = 10$) plate backed with a grounded metal. Here the APPJ operates at 600 Torr and has a N_2 shroud to guide the IW. Due to other experimental requirements, the APPJ remained in a normal orientation while the orientation of the surface was rotated. The images shown in Fig. 9 are for $\theta_J = 0$, 22 and 45°, and display total optical emission. The top of each frame is at the end

of the plasma tube. Other than differences in buoyancy forces, which are not important for these conditions, these results are equivalent to having the surface flat and rotating the jet. For normal incidence, the IW strikes and charges the surface, producing a SIW which spreads laterally along the surface, nearly equally in both directions. The most intense emission occurs at the surface and a few mm above the surface as the IW first strikes and begins to charge the surface.

With the surface oriented at $\theta_J = 22°$, the IW propagates vertically and coaxially with the plasma tube until approximately 2 mm above the surface. At this point, the IW turns to propagate nearly perpendicularly to the surface. Upon striking the surface, a SIW was initiated which spreads more rapidly and further on the downstream side of the jet than the upstream. (Given the orientation of the plate, the RGM plume will preferentially flow towards the right, downstream.) The displacement of the jet is about 0.3 mm. Increasing θ_J to 45°, the IW also propagates vertically, coaxially with the plasma tube until approaching approximately 2.5 – 3 mm of the surface. At that point, it turns to an orientation perpendicular to the surface. With the RGM plume directed to the right, the SIW spreads preferentially downstream where the molecular gas mole fraction in the boundary layer will be smaller than in the upstream boundary layer. The brightest emission occurs within a few mm of the surface as the dielectric charges. The displacement of the jet when striking the surface is 1.5 mm. The results of the simulations correlate well with these experimental trends.

V. RONS Formation as a Function of Angle of the Jet

The formation of RONS in the gas phase that are delivered to a surface being treated can be very broadly divided into primary species and secondary species. Primary species are those that are produced by direct electron impact of the feedstock or ambient gases. These would include O (electron impact on O_2 and H_2O), $O_2(^1\Delta)$ (from O_2), H and OH (from H_2O) and N (from N_2). The primary species may include ions if the active plume, for example, touches the surface. With the exception of $O_2(^1\Delta)$, the majority of primary excited states will have decayed or quenched before reaching the surface. The production of N atoms is small compared to the other primary species, and so the majority of primary species are ROS. The secondary species are those that result from reactions (or a series of reactions) initiated by the primary species. The major ROS secondary species include O_3, H_2O_2 and HO_2. The major RNS secondary species are NO_x and HNO_x, the latter requiring several sequential reactions to form. The secondary species are dominated by RNS.

A major distinguishing characteristic of the primary (ROS dominated) and secondary (RNS) dominated species is residence time required for their generation. The primary species are produced on the time scale of the IW wave (ns to tens of ns) and are less sensitive to the details of the flow field. The secondary species, requiring up to tens of ms to form, are sensitive to their residence time in the flow field.

The densities of OH, a primary RONS, for $\theta_J = 6°$, 28° and 45° are shown in Fig. 10 after 100 plasma pulses at 10 kHz (0.01 s elapsed time). The sum of the densities of secondary N_xO_y and HNO_y species [referred to as $H(N_xO_y)$] for the same angles are shown in Fig. 11. The majority of OH (Fig. 8) is initially generated in the path of the ionization wave as the wave

intersects water vapor, and in the path of the SIW that propagates along the surface of the water through the saturated water vapor. After this initial production, the distribution of OH is determined by its depletion by gas phase reactions, solvation into the water and translation with the gas flow. Since the lifetime of OH is on the order of the residence time of the gas in the computational domain, the spatial distribution generally reflects the flow streamlines.

The time required to generate $H(N_xO_y)$ from its N, O and OH precursors generally exceeds the average residence time of gas in the domain. Those regions that vortex and have longer than average residence times will have more opportunity for reactions between the precursors, which produces larger densities of $H(N_xO_y)$ closer to the water surface. This proximity to the water layer then enables solvation into the water. Regions that do not vortex and have smaller than average residence times will exhaust the precursors before $H(N_xO_y)$ is formed. As the angle of the jet increases, there is more lateral flow across the water surface on the right side, shortening the residence time and dramatically decreasing the formation of $H(N_xO_y)$. Vortex formation on the left side increases the residence, and so enables the formation of $H(N_xO_y)$.

The activation of the water layer by plasma produced species is a complex process that starts with the formation of gas phase RONS, ions and electrons, followed by their transport and solvation into the liquid. Photolytic processes at the surface of the liquid due to plasma produced UV/VUV photons also produce in-water RONS. The angle of the plasma jet affects all of these initiating processes, and so one would expect some systematic ability to control the activation of the water layer by varying the angle of the plasma jet. (In the following $RONS_{aq}$, ROS_{aq} and RNS_{aq} refer to in-liquid densities.)

To investigate the possibility of angle-base control of in-liquid densities, 100 plasma pulses at 10 kHz (0.01 s elapsed time) were simulated and the final inventory of $RONS_{aq}$ was determined. (Inventory is the volume integral of densities.) The resulting inventories for ROS_{aq} and RNS_{aq} are shown in Fig. 12 as a function of the angle of the jet. Values are relative to those obtained at normal incidence. At moderate angle, $\theta_J < 20°$, the inventory of ROS_{aq} is not particularly sensitive to the angle of the jet. The majority of the ROS_{aq} are produced by contact of the plasma with the surface of the water and subsequent SIW. ROS_{aq} is produced directly in the water by charge exchange from plasma species to the water, solvation of O and OH produced in the boundary layer and photolysis reactions. The interactions of the IW and subsequent SIW with the water do not significantly change over this range of angle. As θ_J exceeds 20°, the gas dynamics, on the average, shorten the gas residence of volumetrically produced ROS (e.g., H_2O_2, HO_2, O_3), which reduces their likelihood to solvate and reduces the inventory of ROS_{aq}.

With lower gas phase densities of ROS, the likelihood for de-solvation of ROS_{aq} increases. This is particularly the case for O_3 and O_{3aq}. The production of O_{3aq} underneath the jet is dominated by the solvation of atomic O from the gas phase, which then attaches to dissolved O_{2aq}. With O_3 having a low Henry's Law constant, 0.3, O_{3aq} becomes super-saturated. The supersaturated O_{3aq} then desolvates into the gas phase. With lower O_3 densities at high θ_J, the rate of desolvation of O_{3aq} is larger.

The inventory of RNS_{aq} is initially more sensitive to θ_J than ROS_{aq}. The production of RNS_{aq} is dominated by solvation of $H(N_xO_y)$. With the production of $H(N_xO_y)$ being sensitive to

residence time, which on the average decreases as θ_J increase, the solvation of $H(N_xO_y)$ decreases and so the production of RNS_{aq} decreases. The creation of vortices at large θ_J which stabilizes the residence time ultimately also stabilizes solvation of $H(N_xO_y)$ and production of RNS_{aq}.

The dependence of the inventories of RNS_{aq} and ROS_{aq} on angle of the jet, θ_J, are different over a large range of angle. For example, the ratios of the inventories of RNS_{aq} to ROS_{aq} as a function of angle are shown in Fig. 12. This dependency provides an opportunity to use θ_J as a control mechanism to vary the relative doses of RNS_{aq} and ROS_{aq} delivered to the water layer.

VI. Concluding Remarks

Atmospheric pressure plasma jets (APPJs) consisting of rare gas mixtures (RGM) flowing into ambient air are often described as guided streamers or guided ionization waves. This description acknowledges that the ionization wave forming the plasma preferentially propagates through the RGM where the E/N required to sustain the wave is smaller than in the molecular gas ambient. Given these conditions, the gas dynamics of the RGM plume are important with respect to both the propagation of the IW and the formation of reactive oxygen and nitrogen species (RONS). These gas dynamics may become complex when the APPJ is directed towards a solid or liquid surface. In this regard, the angle of the APPJ (tube) with respect the surface is an important control parameter.

The propagation of IWs for guided (RGM flowing into ambient) and unguided (entire domain consisting of RGM) APPJs were compared as a function of angle of the plasma tube, θ_J. Within the plasma tube, the IW propagated the same for guided and unguided APPJs. The IW progressively followed the contour of the tube as a SIW with an increase in θ_J. As ionization waves exited the tube in the unguided systems, the IWs quickly reoriented to generally follow the vacuum electric fields, becoming progressively oriented perpendicular to the surface. In the absence of gas composition produced gradients in electron impact and transport coefficients, there is no intrinsic confinement of the IW. The displacement of the IW from the extended axis of the tube increases with θ_J. With guided IWs, the larger E/N required to avalanche the ambient air surrounding the RGM plume was able to confine the IW wave up to angles of $\theta_J = 45°$, the largest investigated. The gas dynamics of the RGM plume intersecting with the surface produce a larger volume of RGM dominated gas. The conductive column behind the IW produces compression of the applied potential in front of the IW. Combined, these outcomes enable the IW to be redirected vertically towards the surface within a few mm of the surface and avalanche gas having a larger molecular mole fraction.

The gas dynamics as a function of θ_J systematically vary the production and distribution of ROS and RNS. With ROS largely being primary reactants (or at most requiring one or two heavy particle collisions to form) and RNS largely being secondary reactants (requiring 3-5 collisions to form), the residence time of these species affect their formation, transport to the liquid layer and eventual solvation. The inventories of ROS_{aq} and RNS_{aq} behave differently as a function of θ_J, enabling the angle of the jet to be a control mechanism for activating surfaces and liquids.

Although only He plasma jets were investigated here, we expect that plasma jets sustained in other rare gases will display similar trends. However, a likely systematic trend is that there will be slower diffusion of the ambient air into the plumes of heavier rare gases. This would extend confinement of the plasma plume closer to the surface, and result in a smaller displacement of the jet striking the surface relative to the projected axis of the tube.

A requirement for all such control schemes is having adequate sensors and algorithms to convert the sensor data to an actuator setting – in this case, the angle of the jet. Control will be particularly challenging for these systems. These challenges include having an inexpensive, non-intrusive diagnostic that measures the desired outcome (e.g., RNS_{aq}) and having a control algorithm that is extremely robust. Given that the gas dynamics of these systems are sometimes unstable and sensitive to surface conditions, the control algorithm will need to be applicable over a wide range of conditions. Significant advances have been made in machine learning (ML) based control of plasma jets [28]. It would be challenging to use ML for the control algorithm as a large training set would be required while the recommended actions may not apply outside the training set. This appears to be opportunity for using physics-guided ML.

Data Availability

The data that support the findings of this study are available from the corresponding author upon reasonable request.

Acknowledgements

The authors are appreciative of Dr. Edward V. Barnat for his guidance and for the use of his laboratory for the experimental measurements. This material was based upon work supported by the U.S. Department of Energy, Office of Science, Office of Fusion Energy Sciences under award numbers DE-SC000319 and DE-SC0020232, the US Department of Energy Office of Science Graduate Student Research Program, the National Science Foundation (PHY-1902878) and the NSF Graduate Research Fellowship Program. Sandia National Laboratories is a multimission laboratory managed and operated by National Technology and Engineering Solutions of Sandia, LLC, a wholly owned subsidiary of Honeywell International Inc., for the U.S. Department of Energy's National Nuclear Security Administration under contract DE-NA0003525. This paper describes objective technical results and analysis. Any subjective views or opinions that might be expressed in the paper do not necessarily represent the views of the U.S. Department of Energy or the United States Government.

References

1. A. Khlyustova, C. Labay, Z. Machala, M-P. Ginebra and C. Canal, Front. Chem. Sci. Eng. **13**, 238 (2019).
2. E. R. W. Van Doremaele, V. S. S. K. Kondeti and P. J. Bruggeman, Plasma Source Sci. Technol. **27**, 095006 (2018).
3. X. Lu, G. V. Naidis, M. Laroussi and K. Ostrikov, Phys. Reports **540**, 123 (2014).
4. S. Iseni, A. Schmidt-Bleker, J. Winter, K.-D. Weltmann, and S. Reuter, J. Phys. D. Appl. Phys. **47**, 152001 (2014).
5. Y. Xian, P. Zhang, X. Pei and X. Lu, IEEE Trans. Plasma Sci. **42**, 10 (2014).
6. A. M. Lietz, E. Johnsen and M. J. Kushner, Appl. Phys. Lett. **111**, 114101 (2017).
7. M. Boselli, V. Colombo, E. Ghedini, M. Gherardi, R. Laurita, A. Liguori, P. Sanibondi, and A. Stancampiano, Plasma Chem. Plasma Proc. **34**, 853 (2014).
8. E. Robert, T. Darny, S. Dozias, S. Iseni and J. M. Pouvesle, Phys. Plasma **22**, 122007 (2015).
9. R. D. Whalley and J. L. Walsh, Sci. Report **6**, 31756 (2016).
10. E. Simoncelli, A. Stancampiano, M. Boselli, M. Gherardi and V. Colombo, Plasma **2**, 369 (2019).
11. R. Wild, T. Gerling, R. Bussiahn, K-D. Weltmann and L. Stollenwerk, J. Phys. D: Appl. Phys **47**, 042001 (2014).
12. E. Silkboer, O. Guaitella and A. Sobota, Plasma Source Sci. Technol. **25**, 03LT04 (2016).
13. E. Siklboer, P. Viegas, Z. Bonaventura, E. Garcia-Caurel, A. Sobota, A. Bourdon and O. Guaitella, Plasma Source Sci. Technol. **28**, 096016 (2019).
14. V. V. Kovačević, G. B. Sretenović, E. Slikboer, O. Guaitella, A. Sobota' and M. M. Kuraica, J. Phys. D: Appl. Phys. **51**, 065202 (2018).
15. J. Jiang and P. J Bruggeman, J. Phys. D: Appl. Phys. **53**, 28LT01 (2020).
16. X. Damany, S. Pasquiers, N. Blin-Simiand, G. Bauville, B. Bournonville, M. Fleury, P. Jeanney and J. S. Sousa, Eur. Phys. J. Appl. Phys. **75**, 24713 (2016).
17. T. M. C. Nishime, R. Wagner and K. G. Kostov, Polymers **12**, 1028 (2020).
18. M. Hosseinpour, A. Zendehnam, S. M. H. Sangdehi and H. G. Marzdashti, J. Theoretical Appl. Phys. **13**, 329 (2019).
19. E. Slikboer, A. Sobota, O. Guaitella and E. Garcia-Caurel, J. Phys. D: Appl. Phys. **51**, 115203 (2018).
20. S. A. Norberg, E. Johnsen, M. J. Kushner, Plasma Sources Sci. Technol. **24**, 35026 (2015).
21. S. A. Norberg, G. M. Parsey, A. M. Lietz , E. Johnsen and M. J. Kushner, J. Phys. D: Appl. Phys. **52**, 015201 (2019).
22. A. M. Lietz and M. J. Kushner, Plasma Sources Sci. Technol. **27,** 105020 (2018).
23. J. Kruszelnicki, A. M. Lietz and M. J. Kushner, J. Phys. D: Appl. Phys. **52**, 355207 (2019).

24. S. Mohades, A. M. Lietz, J. Kruszelnicki and M. J. Kushner, Plasma Process Polym. **17**, e1900179 (2020).
25. A. M. Lietz, E. V. Barnat, J. E. Foster, and M. J. Kushner, J. Appl. Phys. **128**, 083301 (2020).
26. Z. Xu, H. Hangan and P. Yu, ASME. J. Appl. Mech. **75**, 021019 (2008).
27. S.L. Arsenjev, arXiv:0801.4160 [physics.flu-dyn]
28. A. Mesbah and D. B. Graves, J. Phys. D: Appl. Phys. **52**, 30LT02 (2019).

Figure Captions

1. Schematic of the computational domain. The plasma jet consists of a quartz tube having a central electrode, oriented at an angle θ_j from the vertical, through which a He/O_2=99.8/0.2 gas mixture at 1 atm is flowed. As the angle is varied, the bottom of the tube is kept at the same location. A humid air shroud flows from the top boundary with gas outlets at both sides. The bottom surface is electrically grounded, covered either a 200 μm water layer or a dielectric having relative permittivity $\varepsilon_r = 80$.

2. Electron density for unguided jets (entire domain is a He/O_2=99.8/0.2 gas mixture) for a -15 kV voltage pulse at the time the ionization wave intersects with the bottom dielectric for tube for angles, θ_j, of a) 6°, b) 28°, c) 40° and d) 51°. The time and maximum electron density are noted in each frame. The densities are plotted over 3-decades on a log-scale.

3. Electron impact ionization source for unguided jets (entire domain is a He/O_2=99.8/0.2 gas mixture) for different times following the start of a -15 kV voltage pulse. The ionization sources are shown as color contours plotted over 3-decades on a log-scale, with the maximum value noted in each frame. The electric potential is also plotted as line-contours, labeled with the potential in kV. Images are shown for the tube oriented at an angle of a) θ_j = 6° and b) θ_j = 51°.

4. Displacement of the plasma jets as a function of the angle of the plasma tube, θ_j. The displacement is the location of the IW striking (or approaching) the surface relative to the extended axis of the plasma tube. A zero displacement indicates that the IW propagates directly along the extended axis of the plasma tube. Values are shown for the unguided jets when the IW strikes the bottom surface, and for the guided jets when the IW strikes the bottom surface (0 mm) and at a height 2.5 mm above the surface.

5. Neutral gas densities and flow field prior to applying the voltage pulse for the guided jets with He/O_2=99.8/0.2 flowing through the tube with a humid air shroud. The APPJ is directed towards an evaporating water covered surface. a) He, b) O_2 and c) H_2O. The densities of He and O_2 are plotted on linear scales and the H_2O density is plotted on a 2-decade log scale with the maximum value shown in each frame. Flow streamlines beginning in the tube are shown in the He images. The orientations of the jet (left to right) are θ_j = 6°, 28° and 40°.

6. Electron density for guided jets (He/O_2=99.8/0.2 gas mixture flowed through the tube into a humid air ambient) for a -15 kV voltage pulse at the time the ionization wave (IW) intersects with the water layer for tube angles, θ_j, of 6°, 22°, 28°, 40°, and 45°. The time and maximum electron density are noted in each frame. The densities are plotted over 3-decades on a log-scale. The single black contour line is where the gas density is 90% He and 10% molecular gases.

7. Electron impact ionization source for guided jets (He/O_2=99.8/0.2 gas mixture flowed through the tube into a humid air ambient) for different times following start of a -15 kV voltage pulse. The ionization sources are shown as color contours plotted over 3-decades on

a log-scale, with the maximum value noted in each frame. The electric potential is also plotted as line-contours, labeled with the potential in kV. The single dashed black line contour is where the density is 90% He and 10% molecular gases. Images are shown for the tube oriented at an angle of a) $\theta_j = 6°$ and b) $\theta_j = 45°$.

8. Electron density and electric field vectors for the guided jet with θ_j, = 45° for different times after the start of the -15 kV voltage pulse – 10, 20, 30 and 40 ns. The electron density is shown as color contours on a 3-decade log-scale with a maximum value of 4×10^{12} cm^{-3}. The electric field vectors have lengths proportional to their magnitude, with the 50 Td arrow shown for scale. The single red contour line is where the density is 90% He and 10% molecular gases.
9. ICCD imaging of total plasma optical emission for a He APPJ (600 Torr) having an N_2 shroud for different angles of incidence onto a dielectric surface. a) 0°, b) 22°, c) 45°. The emission is separately normalized for each angle of incidence and is plotted over a 2-decade log-scale. The times are relative to when the emission appears at the top of the frame, corresponding to the bottom of the plasma tube.
10. Densities of OH radicals following 100 discharge pulses at 10 kHz for jet angles of θ_j of a) 6°, b) 28° and c) 40°. The densities are plotted on a 3-decade log-scale with the maximum density shown in each frame.
11. Densities of $H(N_xO_y)$ species (sum of N_xO_x and HNO_x species) following 100 discharge pulses at 10 kHz for jet angles of θ_j of a) 6°, b) 28° and c) 40°. The densities are plotted on a 2-decade log-scale with the maximum density shown in each frame.
12. Inventories of in-liquid ROS_{aq} and RNS_{aq} at the end of 100 discharge pulses at 10 kHz as a function of the angle of the jet nozzle, θ_j. The inventories are the volume integral of densities in the liquid. Inventories of ROS_{aq} and RNS_{aq} are separately normalized by the value at θ_j = 0. The ratio of RNS_{aq} to ROS_{aq} is also shown.

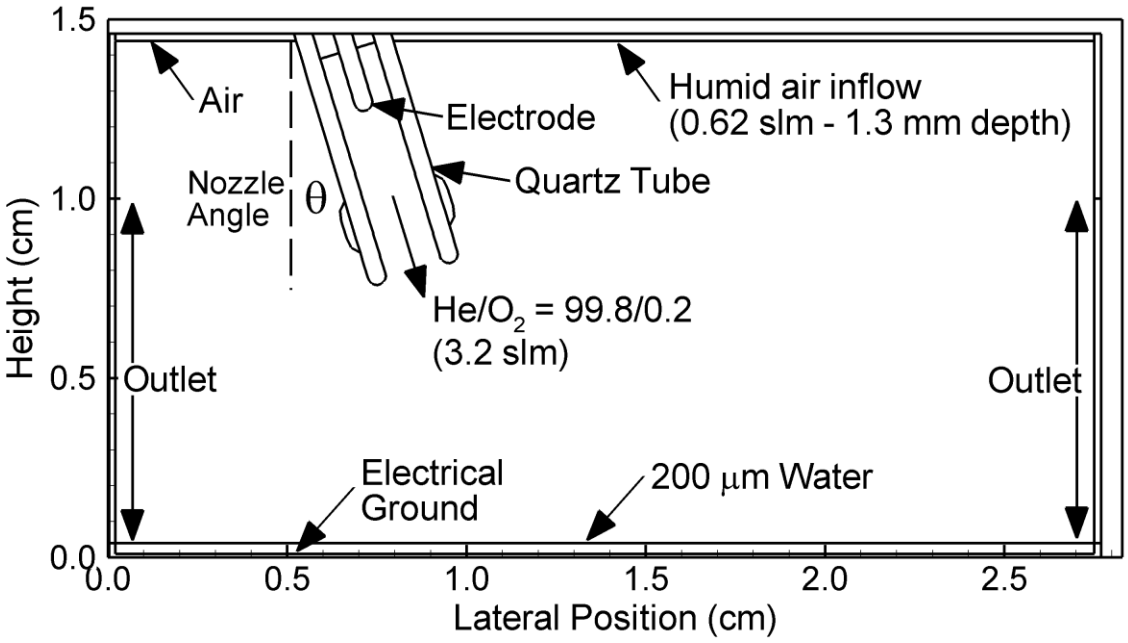
1.5
1.0
0.5
0.0
Height (cm)
Air
Electrode
Humid air inflow
(0.62 slm - 1.3 mm depth)
Nozzle
Angle
θ
Quartz Tube
He/O2 = 99.8/0.2
(3.2 slm)
Outlet
Outlet
Electrical
Ground
200 μm Water
0.0
0.5
1.0
1.5
2.0
2.5
Lateral Position (cm)

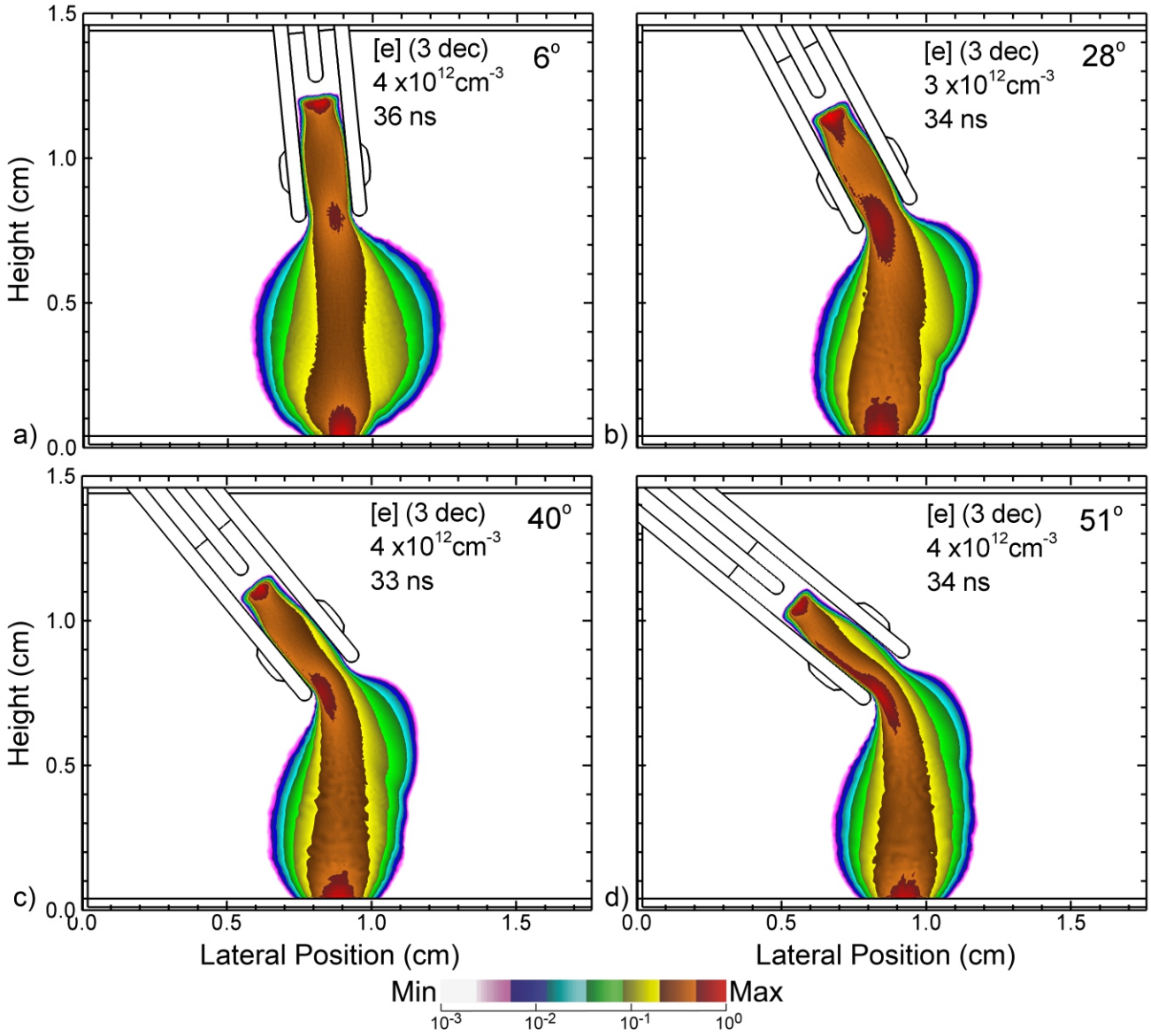
[e] (3 dec)
4 x10^12cm^-3
36 ns
6°
a)
[e] (3 dec)
3 x10^12cm^-3
34 ns
28°
b)
[e] (3 dec)
4 x10^12cm^-3
33 ns
40°
c)
[e] (3 dec)
4 x10^12cm^-3
34 ns
51°
d)
Height (cm)
Lateral Position (cm)
0.0
0.5
1.0
1.5
Min
Max
10^-3
10^-2
10^-1
10^0

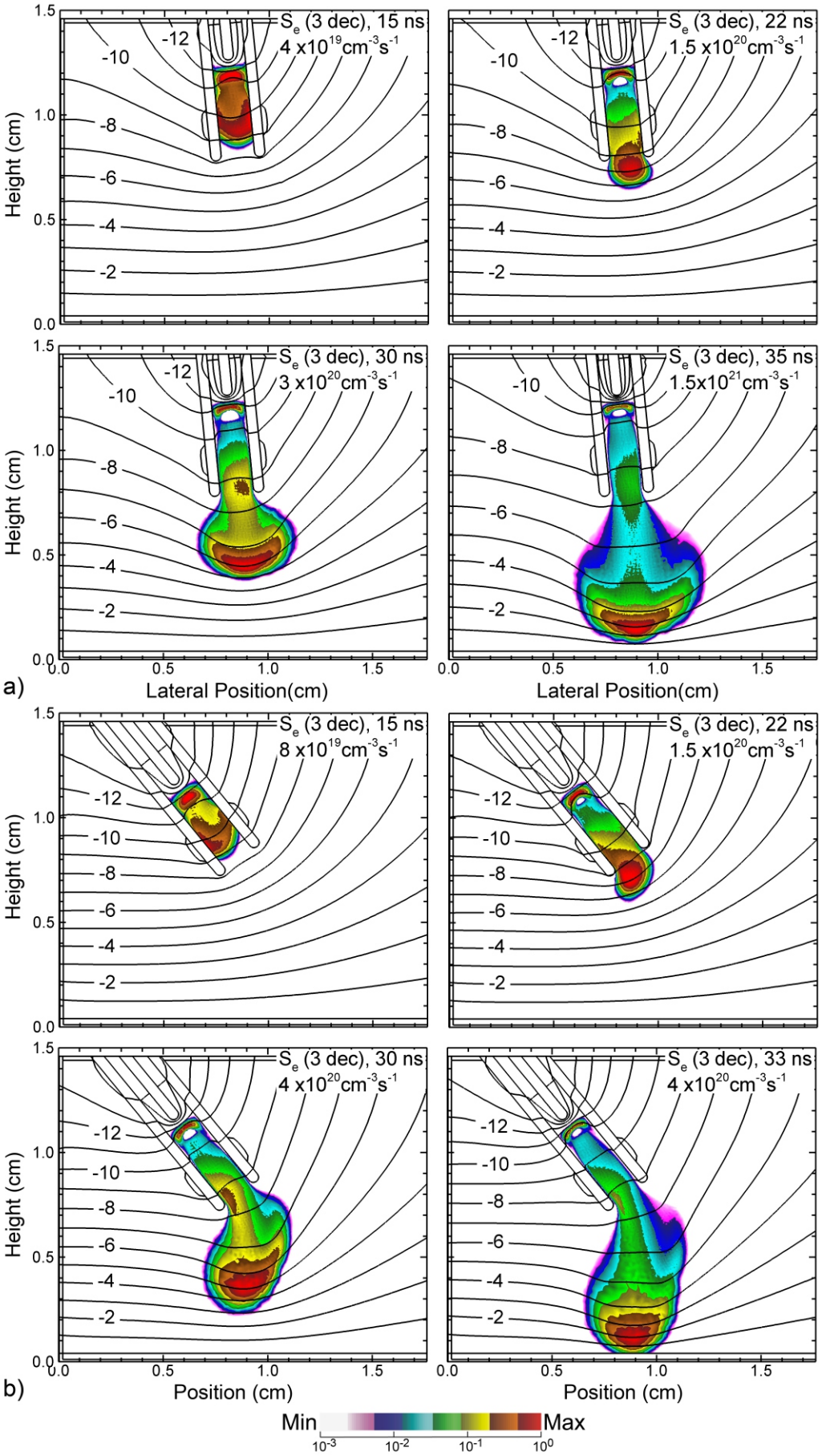

Parsey et al
Figure 3 of 12

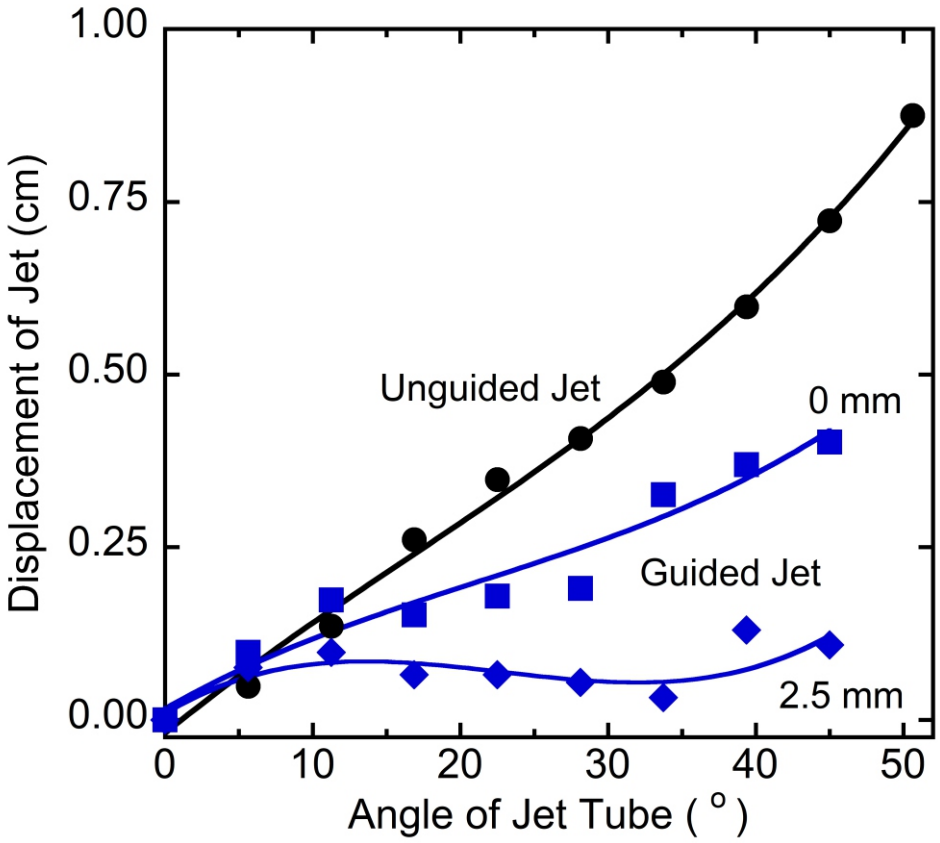
1.00
0.75
0.50
0.25
0.00
Displacement of Jet (cm)
0
10
20
30
40
50
Angle of Jet Tube (°)
Unguided Jet
0 mm
Guided Jet
2.5 mm

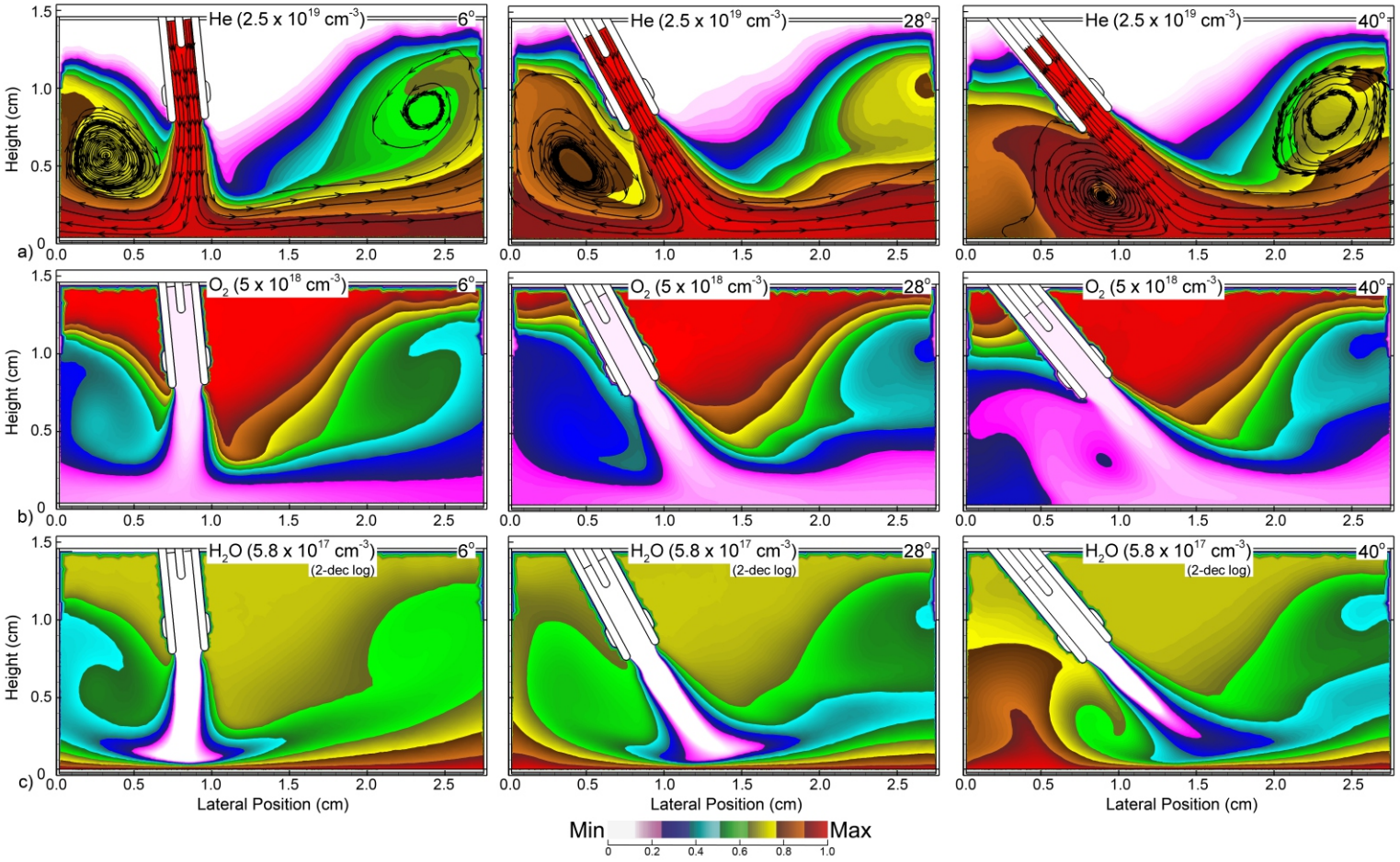

Parsey et al
Figure 5 of 12

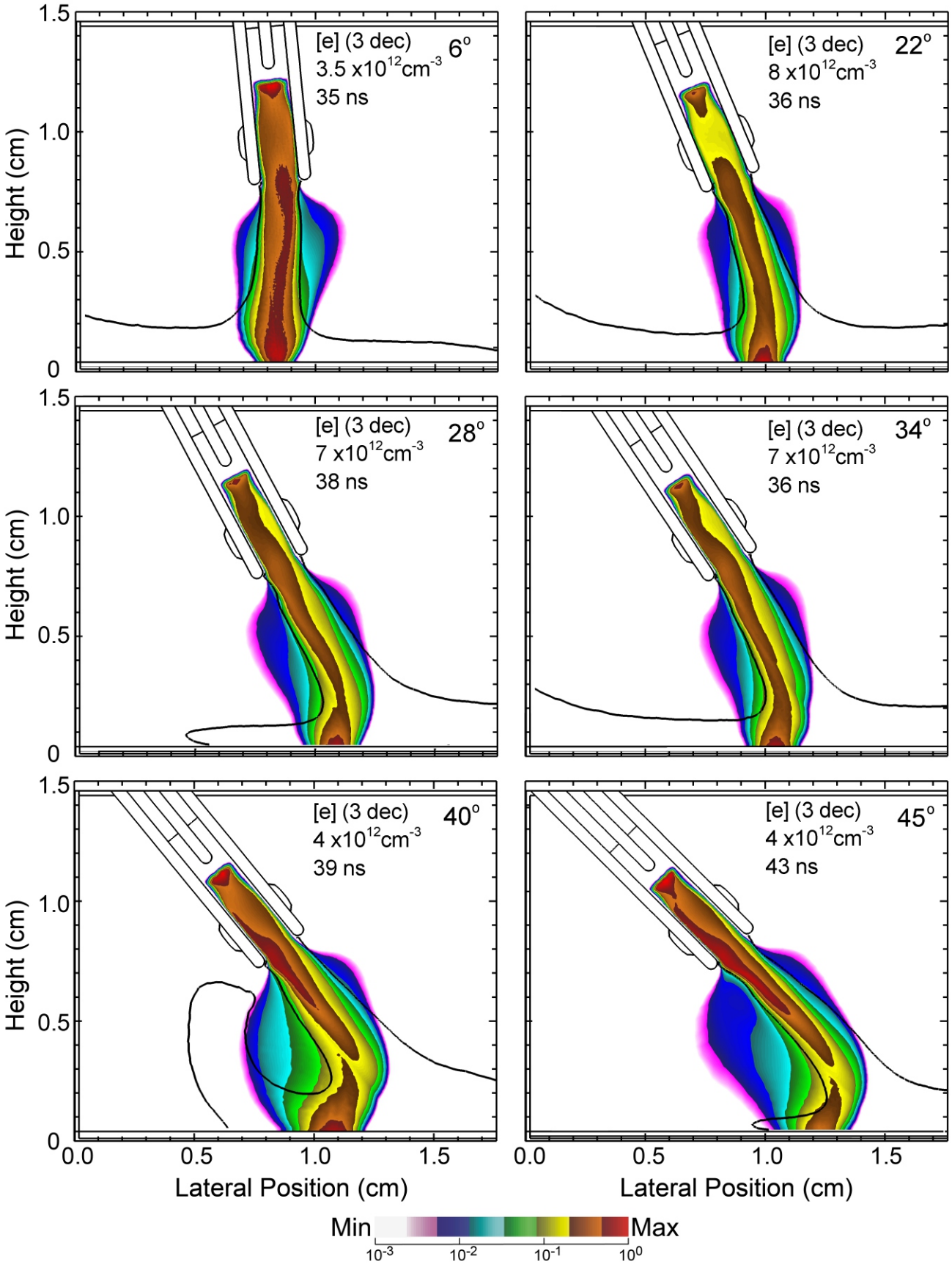
[e] (3 dec)
3.5 x10^12cm^-3
35 ns
6°
[e] (3 dec)
8 x10^12cm^-3
36 ns
22°
[e] (3 dec)
7 x10^12cm^-3
38 ns
28°
[e] (3 dec)
7 x10^12cm^-3
36 ns
34°
[e] (3 dec)
4 x10^12cm^-3
39 ns
40°
[e] (3 dec)
4 x10^12cm^-3
43 ns
45°
Height (cm)
Lateral Position (cm)
0
0.5
1.0
1.5
Min
Max
10^-3
10^-2
10^-1
10^0

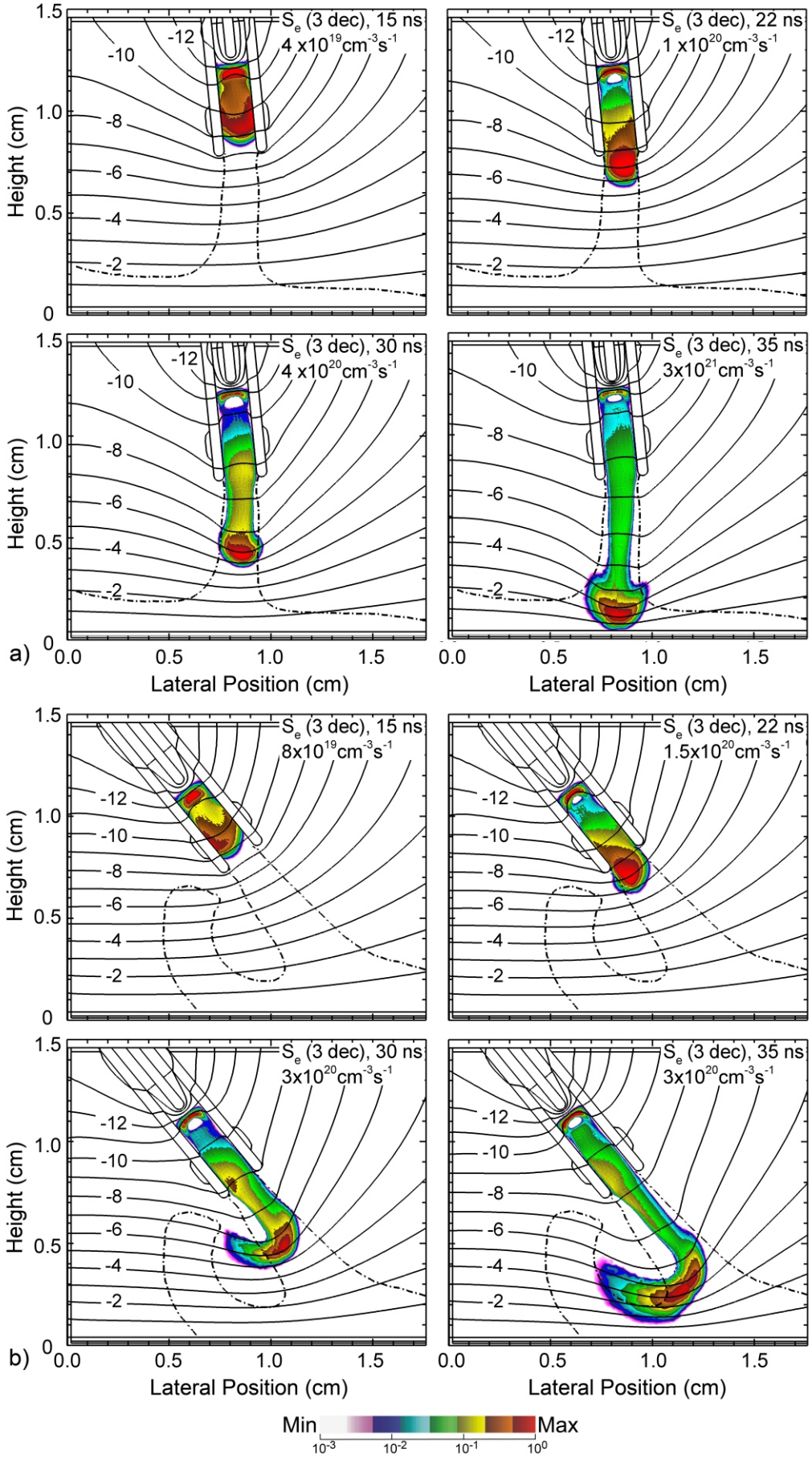

Parsey et al
Figure 7 of 12

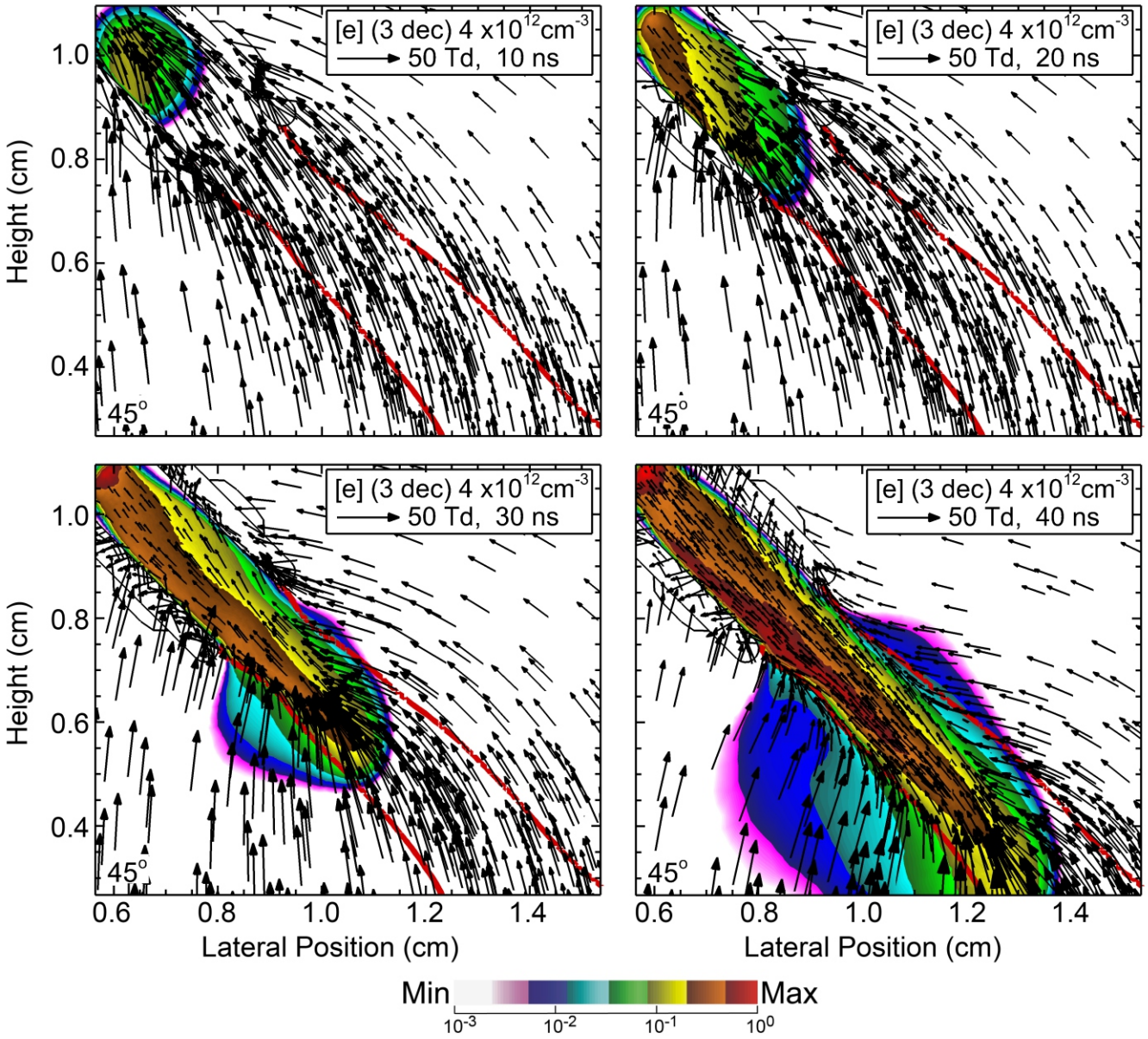
[e] (3 dec) 4 x10^12cm^-3
50 Td, 10 ns
[e] (3 dec) 4 x10^12cm^-3
50 Td, 20 ns
[e] (3 dec) 4 x10^12cm^-3
50 Td, 30 ns
[e] (3 dec) 4 x10^12cm^-3
50 Td, 40 ns
45°
Height (cm)
1.0
0.8
0.6
0.4
0.6
0.8
1.0
1.2
1.4
Lateral Position (cm)
Min
Max
10^-3
10^-2
10^-1
10^0

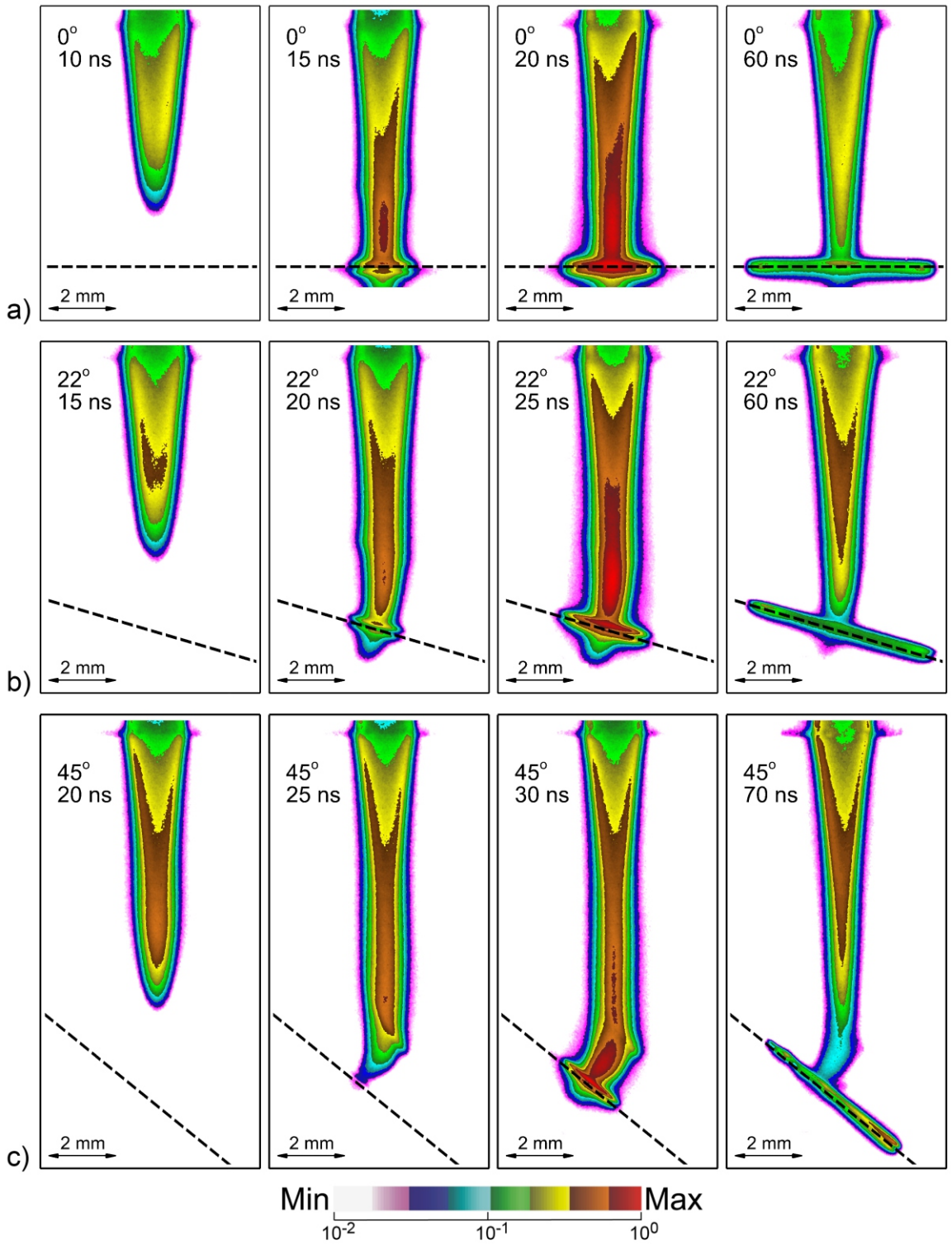
a)
0°
10 ns
0°
15 ns
0°
20 ns
0°
60 ns
2 mm
b)
22°
15 ns
22°
20 ns
22°
25 ns
22°
60 ns
2 mm
c)
45°
20 ns
45°
25 ns
45°
30 ns
45°
70 ns
2 mm
Min
Max
10-2
10-1
100

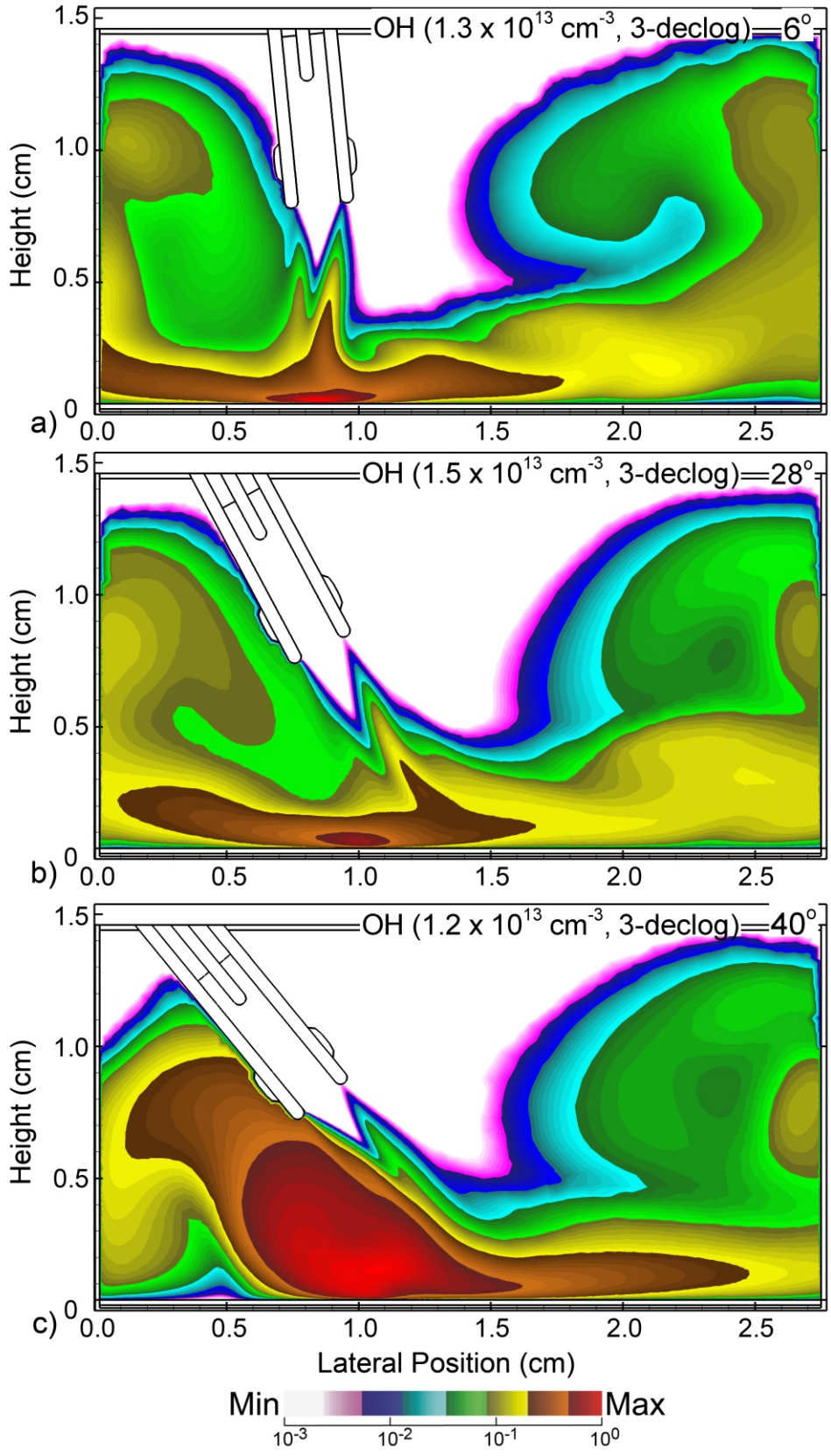
OH (1.3 x 10^13 cm^-3, 3-declog)=6°
OH (1.5 x 10^13 cm^-3, 3-declog)=28°
OH (1.2 x 10^13 cm^-3, 3-declog)=40°
Height (cm)
Lateral Position (cm)
a)
b)
c)
0.0
0.5
1.0
1.5
2.0
2.5
Min
Max
10^-3
10^-2
10^-1
10^0

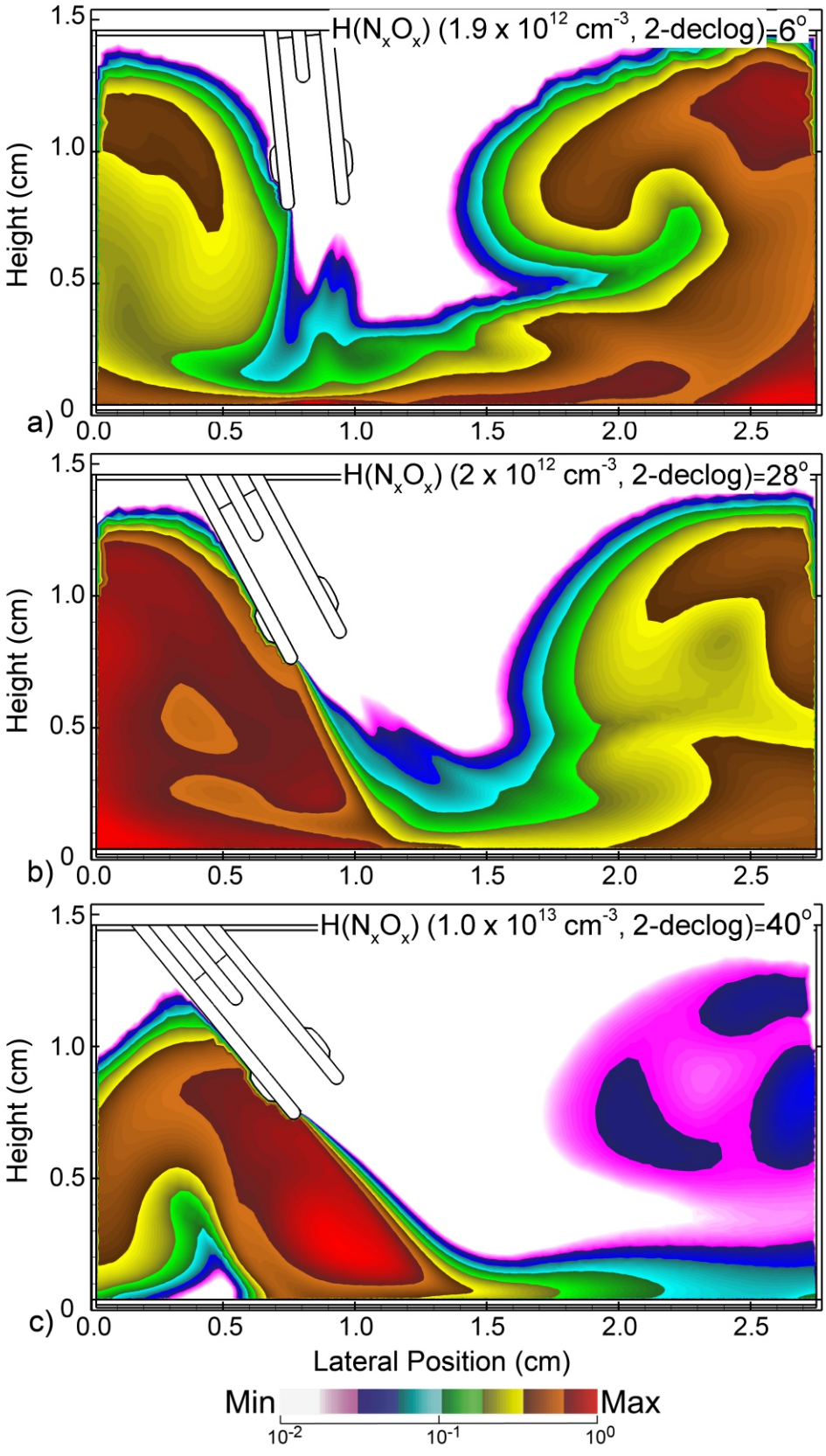

Parsey et al
Figure 11 of 12

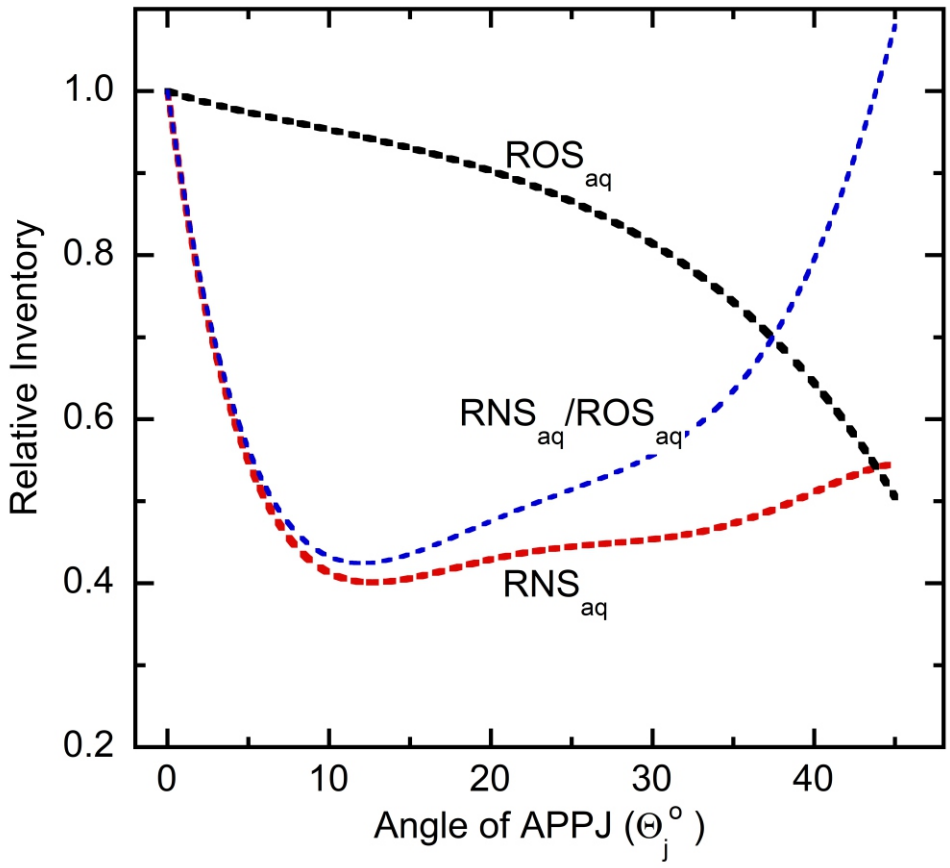
Relative Inventory
1.0
0.8
0.6
0.4
0.2
0
10
20
30
40
Angle of APPJ (Θ_j°)
ROS$_{aq}$
RNS$_{aq}$/ROS$_{aq}$
RNS$_{aq}$